Dalton Transactions

Dynamic Article Links

Cite this: *Dalton Trans.*, 2012, **41**, 180

www.rsc.org/dalton

PAPER

Near-UV to red-emitting charged bis-cyclometallated iridium(III) complexes for light-emitting electrochemical cells†

Florian Kessler,[a] Rubén D. Costa,‡[b] Davide Di Censo,[a] Rosario Scopelliti,[a] Enrique Ortí,*[b] Henk J. Bolink,[b] Sebastian Meier,[c] Wiebke Sarfert,[c] Michael Grätzel,[a] Md. Khaja Nazeeruddin[a] and Etienne Baranoff*[a]

Received 18th April 2011, Accepted 8th September 2011
DOI: 10.1039/c1dt10698h

Herein we report a series of charged iridium complexes emitting from near-UV to red using carbene-based N^C: ancillary ligands. Synthesis, photophysical and electrochemical properties of this series are described in detail together with X-ray crystal structures. Density Functional Theory calculations show that the emission originates from the cyclometallated main ligand, in contrast to commonly designed charged complexes using bidentate N^N ancillary ligands, where the emission originates from the ancillary N^N ligand. The radiative process of this series of compounds is characterized by relatively low photoluminescence quantum yields in solution that is ascribed to non-radiative deactivation of the excited state by thermally accessible metal-centered states. Despite the poor photophysical properties of this series of complexes in solution, electroluminescent emission from the bluish-green to orange region of the visible spectrum is obtained when they are used as active compounds in light-emitting electrochemical cells.

Introduction

Light-emitting electrochemical cells (LECs) based on ionic transition-metal complexes (iTMCs) are emerging as a promising alternative to organic light-emitting diodes (OLEDs).[1,2] The major advantages of iTMC-based LECs over OLEDs originate from the use of solution processing and simpler architectures. Moreover, because of the presence of mobile ions under applied voltage, the ions migrate towards the electrodes and assist the charge injection in the device. Multi-layer architectures necessary in OLEDs for charge injection and transport are therefore not necessary in LECs. In addition, air-stable electrodes can be used which allows a non-rigorous encapsulation process. These characteristics make the industrial production of LECs promisingly easier. However, iTMCs-based LECs still present important drawbacks, which mainly concern the efficiency, the turn-on time and the white color emission. To achieve white-light emission in LECs, it is necessary to combine sky-blue and orange emitters in a two-component system or blue, green and red emitters in a three-component system. Stable and efficient orange LECs have been reported.[3–5] Hence, the primary requirement for achieving white-light emission is to prepare ionic blue-emitting complexes. A few examples of blue emitters have been reported; however, their use in LECs has not provided high performances.[6–11]

The typical kind of iTMCs used in LECs are charged bis-cyclometallated iridium(III) complexes which have attracted widespread interest in recent years due to their high phosphorescence quantum yield, relatively short radiative lifetime and wide color tunability.[1,12–15] However, their reported emission wavelength is limited on the blue side of the visible spectrum to about 450 and 440 nm when bidentate and monodentate ancillary ligands are used, respectively. The use of bidentate ancillary ligands forming a five-membered ring with the central metal cation is advantageous over monodentates due to the improved stability provided by the chelation effect. The most common design of charged bis-cyclometallated iridium(III) complexes for LECs is based on a neutral N^N ancillary ligand such as bipyridine,[10,16–19] phenanthroline,[20] pyridine-pyrazole,[7] pyridine-imidazole,[8] pyridine-triazole[9] and pyridine-tetrazole.[21] Blue emission is obtained by introducing ancillary ligands with a higher-energy lowest-unoccupied molecular orbital (LUMO) than bipyridine, as emission originates from the ancillary ligand, and/or by stabilizing the highest-occupied molecular orbital (HOMO) through introduction of electron-withdrawing groups on the orthometallated phenyl ring.[22]

In neutral iridium(III) complexes used in OLEDs, deep-blue emission has been achieved by using carbene-based ligands.[23] In this manuscript we present a strategy based on a neutral

[a]*Laboratory of Photonics and Interfaces, Institute of Chemical Sciences and Engineering, Swiss Federal Institute of Technology, Station 6, CH-1015, Lausanne, Switzerland. E-mail: etienne.baranoff@epfl.ch*
[b]*Instituto de Ciencia Molecular, Universidad de Valencia, 46980, Paterna, Spain. E-mail: enrique.orti@uv.es*
[c]*Siemens AG, Corporate Technology, CT T DE HW3, GTF Organic Electronics, Gunther-Scharowsky Strasse 1, 91058, Erlangen, Germany*
† CCDC reference numbers 822776–822780. For crystallographic data in CIF or other electronic format see DOI: 10.1039/c1dt10698h
‡ Present address: Friedrich-Alexander-Universität Erlangen-Nürnberg, Department of Chemistry and Pharmacy & Interdisciplinary Center for Molecular Materials (ICMM), Egerlandstrasse 3, 91058 Erlangen, Germany.

pyridine-carbene (N^C:) ancillary ligand forming a five-membered ring with the central iridium to prepare a series of charged bis-cyclometallated iridium complexes with emission ranging from near-UV to red. Based on experimental and theoretical data, we reasoned that due to the very high LUMO of the carbene ligand, the emission originates from the main cyclometallated ligand. This can be related to the case of non-chromophoric monodentate ancillary ligands.[24] This design allows a straightforward tuning of the emission maximum of charged iridium(III) complexes using classical tuning strategies on the main C^N ligand. In particular this simple design allows deep-blue emission which is highly desirable for white emitting electroluminescent devices based on three components. LEC devices using some of these compounds as the primary active components show electroluminesce from bluish-green to orange.

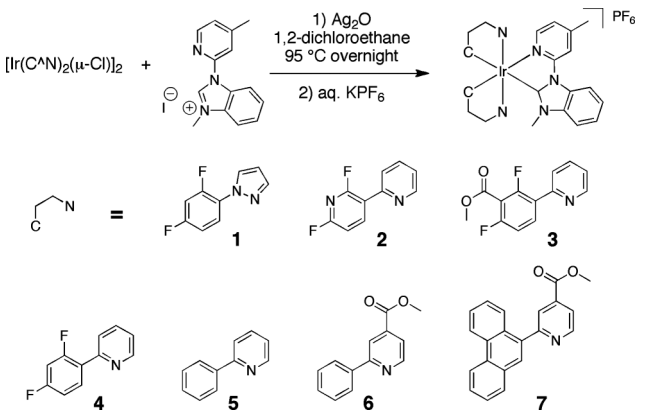

Scheme 1 General synthetic scheme for charged iridium(III) complexes and molecular structures of complexes **1–7**.

Results and discussion

Synthesis

Since the first isolation of a stable N-heterocyclic carbene (NHC) in 1991,[25] numerous stable NHCs have been prepared. In recent years, N-heterocyclic carbenes have evolved into very powerful co-ligands for transition metal complexes. Usually the NHC ligand is introduced into the complexes as an entity starting from either free NHCs or suitable precursors. Another approach would be a stoichiometric transfer of carbene ligands from one metal to another (transmetalation).[26,27] A wide range of transition metals has been used as the carbene donor;[28–31] however, the most common metal for carbene transmetalations is silver.[32,33] To follow this approach, we generated the silver-NHC complex *in situ* from its benzimidazolium precursor. The benzimidazolium iodide ancillary ligand was synthesized by a copper catalyzed N-arylation of benzimidazole with 2-bromo-4-methylpyridine followed by alkylation with methyl iodide.[34,35]

Complexes **1–7** have been synthesized as depicted in Scheme 1. As reported in the literature, the chloro-bridged iridium dimer $[Ir(C^N)_2(\mu\text{-}Cl)]_2$ is easily accessible from commercially available $IrCl_3{\cdot}3H_2O$ and C^N ligand. Then, $[Ir(C^N)_2(\mu\text{-}Cl)]_2$, the benzimidazolium ancillary ligand and Ag_2O were dissolved in 1,2-dichloroethane under nitrogen and the mixture was refluxed overnight. After filtration through celite, the iodine salts of the complexes were extracted with aqueous KPF_6 solution to generate the desired complexes as PF_6 salts, which were further purified by column chromatography on silica and isolated in good to excellent yield (50–95%).

X-ray crystal structures

The X-ray crystal structures of complexes **2**, **3**, **4**, **5** and **6** have been obtained from single crystals grown by slow diffusion of heptane into a dichloromethane solution of the complex (Fig. 1 and Table 1). All of them present similar structural parameters as seen in Table 2. They show a near-octahedral geometry with the two pyridines of the anionic cyclometallated ligands in *trans* position one to each other and the two orthometallated phenyl rings in *cis* position, retaining the geometry of the starting chloro-bridged iridium dimer. In all complexes the bite angle of the pyridine-carbene ancillary ligand is close to 76.5°, which is similar to the bite angle of a bipyridine ancillary ligand.[36] While the iridium–carbon(carbene) distance (Ir–C1 in Table 2) is barely affected by the substitution on the C^N ligand and is about 2.07 Å for all complexes, the iridium–nitrogen(carbene) distance (Ir–N1 in Table 2) is more strongly affected and appears to shorten as the accepting capability of the phenyl in the *trans* position increases. Without substitution (complex **5**), the Ir–N1 bond is 2.169(4) Å and shortens to 2.131(6) Å for complex **2**. Finally, it should be noted that the length of the Ir–C3 bond is in all cases longer than the Ir–C2 bond, reflecting the strong *trans*-effect of the carbene group.

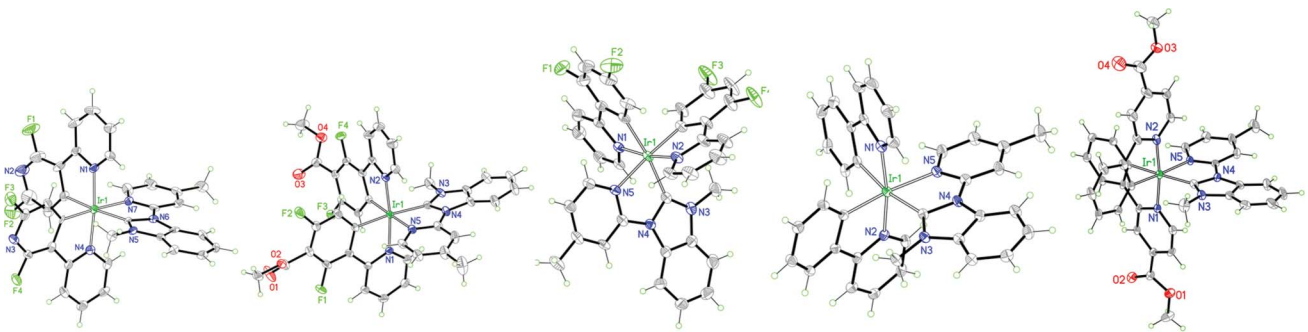

Fig. 1 ORTEP drawings of complexes **2**, **3**, **4**, **5** and **6** (from left to right). PF_6 counterions are omitted for clarity.

Table 1 Crystallographic data for complexes **2**, **3**, **4**, **5** and **6**

	2·(2.5 CH_2Cl_2)	**3**·(CH_2Cl_2)	**4**·(1.25 CH_2Cl_2)	**5**·(2 CH_2Cl_2)	**6**·(2 CH_2Cl_2)
Empirical formula	$C_{36.5}H_{28}Cl_5F_{10}IrN_7P$	$C_{41}H_{31}Cl_2F_{10}IrN_5O_4P$	$C_{37.25}H_{27.5}Cl_{2.5}F_{10}IrN_5P$	$C_{38}H_{33}Cl_4F_6IrN_5P$	$C_{42}H_{37}Cl_4F_6IrN_5O_4P$
Formula weight	1155.08	1141.78	1046.94	1038.66	1154.74
T (K)	100(2)	100(2)	100(2)	100(2)	100(2)
λ (Å)	0.71073	0.71073	0.71073	0.71073	0.71073
Crystal system	Orthorhombic	Triclinic	Triclinic	Monoclinic	Monoclinic
Space group	$Pca2_1$	$P\bar{1}$	$P\bar{1}$	$P2_1/n$	$P2_1/c$
Unit cell dimensions					
a (Å)	18.9854(16)	11.384(2)	12.3624(4)	16.874(2)	12.1292(18)
b (Å)	10.9239(9)	13.3335(12)	18.486(4)	13.0638(19)	22.928(3)
c (Å)	40.018(7)	16.662(3)	18.518(2)	18.0002(14)	17.637(3)
α (°)	90	85.227(14)	84.272(14)	90	90
β (°)	90	89.374(13)	73.057(5)	102.348(8)	100.421(13)
γ (°)	90	68.736(8)	70.988(5)	90	90
volume (Å^3)	8299.6(17)	2348.3(7)	3827.4(9)	3876.1(8)	4823.9(12)
Z	8	2	4	4	4
density, calcd (g cm^{-3})	1.849	1.615	1.817	1.780	1.590
absorption coefficient (mm^{-1})	3.662	3.075	3.790	3.827	3.090
F(000)	4504	1020	2042	2040	2280
Crystal size (mm^3)	0.50 × 0.43 × 0.19	0.45 × 0.36 × 0.27	0.34 × 0.29 × 0.28	0.35 × 0.23 × 0.20	0.40 × 0.30 × 0.20
θ range (deg)	3.05 to 25.02	3.07–27.5	3.27–27.50	3.00–27.50	3.14–27.50
Reflections collected	103 411	42 941	62 064	67 576	49 931
Independent reflections	14 675	10559	16 576	8864	11 050
refinement method	[R(int) = 0.0431] Full-matrix least-squares on F^2	[R(int) = 0.0360] Full-matrix least-squares on F^2	[R(int) = 0.0348] Full-matrix least-squares on F^2	[R(int) = 0.0826] Full-matrix least-squares on F^2	[R(int) = 0.0572] Full-matrix least-squares on F^2
data/restraints/parameters	14 675/59/1118	10 559/174/624	16 576/158/1091	8864/25/524	11 050/0/568
goodness-of-fit on $F2$	1.125	1.095	1.114	1.075	1.132
Final R indices [$I > 2\sigma(I)$]	R_1 = 0.0390	R_1 = 0.0248	R_1 = 0.0316	R_1 = 0.0377	R_1 = 0.0682
R indices (all data)	wR_2 = 0.0870 R_1 = 0.0436 wR_2 = 0.0893	wR_2 = 0.0594 R_1 = 0.0293 wR_2 = 0.0620	wR_2 = 0.0634 R_1 = 0.0510 wR_2 = 0.0731	wR_2 = 0.0810 R_1 = 0.0568 wR_2 = 0.0910	wR_2 = 0.1464 R_1 = 0.0936 wR_2 = 0.1576

Table 2 Selected bond lengths (Å) and angles (°) for complexes **2**, **3**, **4**, **5** and **6**

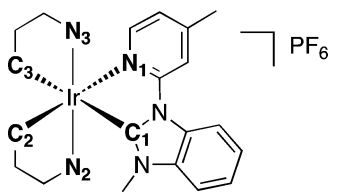

Bond distances	Bond angles	**2**		**3**		**4**		**5**		**6**	
Ir–N1	N1–Ir–C1	2.131(6)	76.4(3)	2.149(3)	76.07(10)	2.153(4)	76.59(16)	2.169(4)	76.21(17)	2.143(6)	76.4(3)
Ir–N2	C3–Ir–C1	2.041(6)	172.8(3)	2.054(2)	170.39(11)	2.058(4)	172.07(17)	2.056(4)	169.09(18)	2.055(7)	170.9(3)
Ir–N3	C2–Ir–C1	2.048(7)	102.4(3)	2.053(2)	104.15(11)	2.063(4)	100.31(19)	2.067(4)	97.31(18)	2.055(7)	102.2(3)
Ir–C1	C2–Ir–C3	2.071(7)	84.7(3)	2.073(3)	85.38(11)	2.064(5)	87.54(19)	2.070(5)	92.41(18)	2.074(8)	86.5(3)
Ir–C2	C3–Ir–N1	2.017(7)	96.6(3)	2.006(3)	94.46(10)	2.010(5)	95.65(16)	2.027(5)	94.26(16)	2.037(8)	95.1(3)
Ir–C3	N3–Ir–N2	2.053(8)	174.0(3)	2.060(3)	171.78(9)	2.053(5)	171.26(15)	2.068(5)	170.36(15)	2.069(7)	172.5(3)

Electrochemical properties

The electrochemical potentials *vs.* ferrocenium/ferrocene of complexes **1–7** are summarized in Table 3. Fig. 2 displays the cyclic voltammograms for the most representative behaviors of this series of complexes: complex **7** (quasi-reversible system), complex **5** (between quasi-reversible and irreversible system) and complex **3** (totally irreversible system for the reduction). While it is expected that oxidation potentials change with the substitution pattern on the main ligand, it is more surprising to see significant behavior differences for the reduction potentials among the complexes.

The oxidation potential of complex **5** (0.86 V) is similar to other $[Ir(ppy)_2(N\hat{}N)]^+$ complexes (N^N = 2-(1*H*-pyrazol-1-yl)pyridine, E_{ox} = 0.87 V;[7] N^N = 1-phenyl-2-(pyridin-2-yl)-1*H*-benzo[*d*]imidazole, E_{ox} = 0.85 V;[8] N^N = 2,2′-bipyridine, E_{ox} = 0.86 V[37]). As for **5**, the oxidation potential for **4** (1.19 V) is almost the same as other $[Ir(2,4\text{-difluoro-ppy})_2(N\hat{}N)]^+$ complexes (N^N = 2-(1*H*-pyrazol-1-yl)pyridine, E_{ox} = 1.20 V;[7] N^N = 1-phenyl-2-(pyridin-2-yl)-1*H*-benzo[*d*]imidazole, E_{ox} = 1.19 V;[8] N^N = pyridine-1,2,3-triazole derivatives, E_{ox} = 1.19–1.26 V[9]). This clearly indicates a similar HOMO localization on both the phenyl ring of the cyclometallated ligands and the iridium center. Indeed,

Table 3 Photophysical and electrochemical properties of complexes **1–7**

	E_{ox} (V)[a]	E_{red} (V)[a]	λ_{abs} (nm) (ε (10^3 M^{-1} cm^{-1}))[b]	λ_{em} (nm)[d]	τ (ns)[d]	Φ_L[d]	λ_{em} (nm), 77 K[e,f]	k_r[g] (10^5 s^{-1})	k_{nr}[g] (10^5 s^{-1})
1	1.20	–2.36*i*	242 (43.0) 274 (30.5) 333sh (2.60) 364sh (0.5)	—	—	—	390	—	—
2	1.61	–2.20*i*	249 (64.0) 282 (37.7) 321 (14.2) 343sh (6.25) 400 (0.1) 425 (0.03)	435	8524	0.197	433 [106]	0.23	0.94
3	1.38	–2.06*i*	250 (72.1) 277 (54.3) 353sh (6.28) 411 (0.22) 435 (0.09)	447	647	0.083	443 [202]	1.28	14.2
4	1.19	–2.26	245 (61.3) 257sh (55.1) 281sh (36.4) 357 (5.73) 414 (0.25) 439 (0.09)	450	249	0.034	446 [199]	1.37	38.8
5	0.86	–2.43	251 (47.3) 266 (44.3) 306sh (18.5) 375 (5.11) 459 (0.11)	471	65	0.009	465 [274]	1.39	152.5
6	0.95	–1.81	251 (56.2) 273 (58.1) 325 (22.5) tail from 400 (5.84) to 509 (0.1)[c]	588	155	0.057	537 [1615]	3.68	60.8
7	0.71	–2.00 –1.74 –1.94	257 (88.5) 278sh (63.3) 326 (33.2) 417 (12.8) 464 (7.18) 610sh (0.05)	663	1569	0.061	635 [665]	0.39	5.98

[a] From CV measurements, $E = 1/2(E_{pa}+E_{pc})$; acetonitrile/$TBAPF_6$ 0.1 M, *vs.* Fc^+/Fc; *i* denotes an irreversible potential. [b] Acetonitrile at room-temperature. [c] Contains several poorly-resolved shoulders. [d] Degassed acetonitrile at room temperature; τ: lifetime of excited state; Φ_L: photoluminescence quantum yield in solution. [e] Tetrahydrofuran. [f] ν_{max}(77 K)–ν_{max}(RT) (cm^{-1}). [g] Calculated using the relations $k_r = \Phi_L/\tau$ and $k_{nr} = 1/\tau - k_r$.

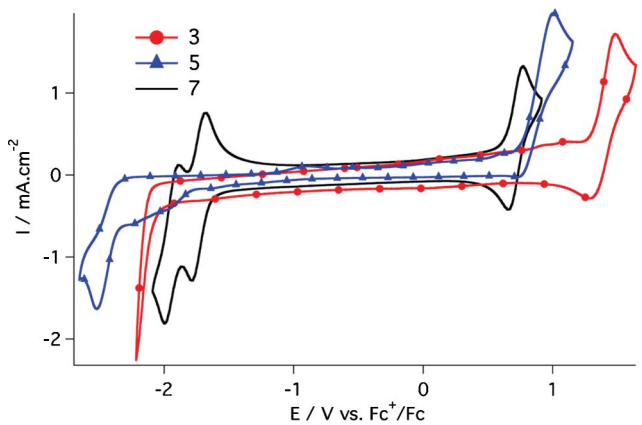

Fig. 2 CVs of complexes **3** (red line), **5** (blue line) and **7** (black line), scan rate 1 V s^{-1}, 3rd scan.

this assumption is well supported by theoretical calculations (see below).

The reduction potentials for charged iridium complexes containing one neutral N^N ancillary ligand are usually practically independent of the substitution pattern of the cyclometallated ligand.[12,13,23,38] However, in the case of this series of complexes, despite having identical ancillary ligands, the reduction potentials are significantly different from one complex to another. These differences are attributed to different substitution patterns on the cyclometallated main ligand. The effect is especially marked for complexes **6** (–1.81 V) and **7** (–1.74 V) compared to complex **5** (–2.43 V). For complexes **2**, **3** and **4**, the electron withdrawing groups on the cyclometallated phenyl affect the reduction potentials as well, as they are stabilized compared to **5**. Finally, the reversibilities of the electrochemical processes differ significantly going from one complex to another as seen in Fig. 2. All this strongly points to the electroactive LUMOs being localized at least partly on the main ligand, in contrast to complexes having an N^N ancillary ligand.

Photophysical properties

UV-visible absorption spectra measured in acetonitrile solution at room temperature (Table 3 and Fig. 3) display strong bands in the UV up to 300 nm attributed to intraligand (π–π^*) transitions. Lower-energy absorption bands correspond to metal-to-ligand charge transfer (MLCT) transitions. Finally, weak bands with ε ~ 100 M^{-1} cm^{-1} are observed clearly for complexes **2**, **3**, **4** and **5** and poorly for **6** and **7**. These bands are ascribed to spin-forbidden transitions directly to triplet states.

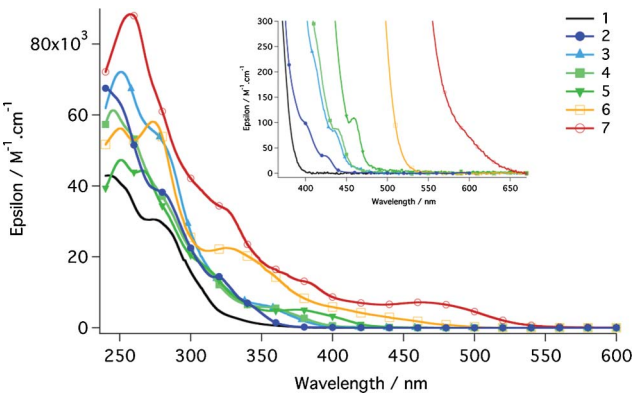

Fig. 3 Absorption spectra of complexes **1–7** in acetonitrile solution at room temperature. Inset: zoom into the absorption bands to triplet states.

When excited at room temperature in the lowest energy ^{1}MLCT band, the complexes show emission with low (Φ_L = 1%) to fair (Φ_L = 20%) photoluminescence quantum yield (Fig. 4 and Table 3). The exception is complex **1** which is non-emitting at room-temperature, as has been observed for the complex $Ir(ppz)_3$.[39] This is additional support for the emission originating from the

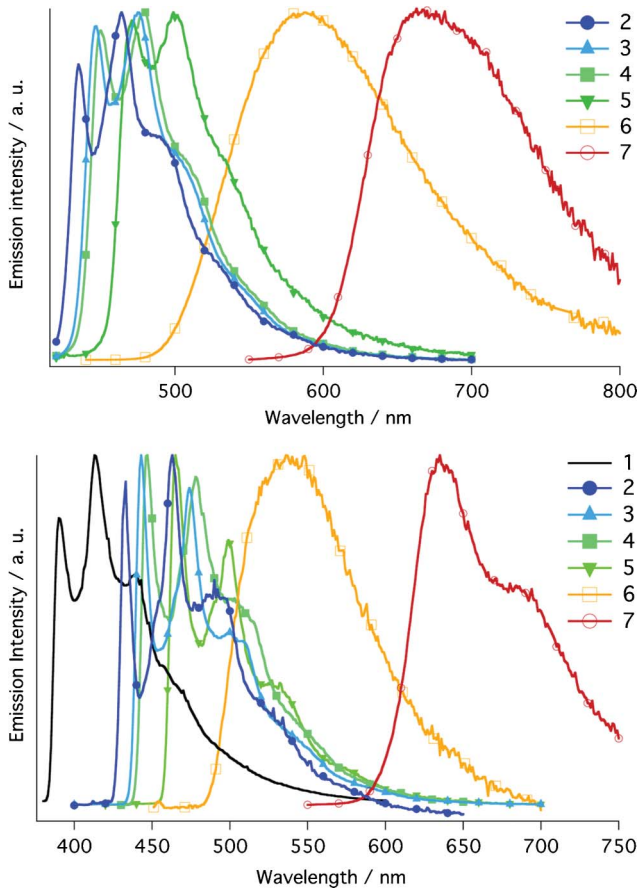

Fig. 4 Photoluminescence of complexes **2–7** at room temperature in MeCN (top) and complexes **1–7** at 77 K in THF (bottom).

main ligand and not from the ancillary ligand. Notably, **2** has the highest-energy emission maxima at 435 nm, significantly blue-shifted compared to commonly obtained blue emitters based on diimine ancillary ligands. While **2**, **3**, **4** and **5** exhibit structured emission spectra at room temperature, **6** and **7** show broad and unstructured emissions, pointing to a higher MLCT character in the excited state of those two complexes. When cooled to 77 K (Fig. 4) complex **1** emits at 390 nm, which is, to the best of our knowledge, the highest-energy-emitting charged iridium complex to date. To verify that this emission does not originate from an external source, excitation of the solvent under the same conditions has been measured and leads to minor background signal with intensity about 10% of the signal measured for **1** and an emission maximum at 379 nm. Compared to room-temperature spectra, complexes **1–5** show structured spectra (Fig. 4) while complexes **6** and **7** present structureless and poorly structured spectra, respectively. The latter complexes have the strongest rigidochromic effect[40] along the series, with ν_{max}(77 K)–ν_{max}(RT) values of ~1600 (**6**) and 650 cm^{-1} (**7**), much larger than the other complexes (Table 3), indicating a more polar structure of the excited state (increased MLCT character) which would explain their emission profiles.

For complexes **3–7**, the excited-state lifetimes (τ) are on the hundred-nanoseconds scale and the photoluminescence quantum yields are only a few percent in acetonitrile at room temperature (Table 3). The radiative rate constant (k_r) is of the order of 10^5 s^{-1} for **3**, **4**, **5** and **6**, while it is of the order of 10^4 s^{-1} for **2** and **7**. These values agree well with calculated values based on the Strickler–Berg relationship[41,42] using the triplet absorption band (Table 4) and are in the range commonly observed for cyclometallated iridium complexes. Therefore, the low photoluminescence quantum yields are attributed to the non-radiative rate constants (k_{nr}) that are at least one order of magnitude larger than the radiative constants. As bright emission is observed at low temperature, non-radiative states are likely thermally accessible at room temperature. These non-radiative states are assigned to metal-centered (^{3}MC) states involving the breaking of coordination bonds, as previously reported,[43,44] and supported by theoretical calculations (see below).

Table 4 Parameters used to calculate k_r from Strickler–Berg equation (I)

Equation (I) $k_r = \frac{1}{\tau_r} = 1.728\times10^{-9}\bar{\nu}^{-2}\varepsilon_{max}\Delta\bar{\nu}_{\frac{1}{2}}$

	$\tilde{\nu}$ (cm^{-1})	ε_{max} (M^{-1} cm^{-1})	$\Delta\bar{\nu}_{\frac{1}{2}}$ (cm^{-1})	k_r calc. (10^5 s^{-1})	k_r exp. (10^5 s^{-1})
2	23 640	34	974	0.32	0.23
3	22 989	84	928	0.71	1.28
4	22 779	87	910	0.73	1.37
5	21 786	109	840	0.76	1.39
6	20 576	644	910	4.29	3.68
7	16 369	51	878	0.21	0.39

Theoretical calculations

Theoretical calculations on the ground and excited states were performed to gain insight into the photo- and electrochemical properties of the complexes. A particular interest was to gain support for the emission originating from the main ligand in contrast to charged iridium complexes having bidentate N^N ancillary ligands, where the emission originates from the ancillary ligand. Calculations have been limited to complexes **3**, **4**, **5** and **6** as representatives of the entire series.

The molecular structures of complexes **3–6** were investigated by performing DFT calculations at the B3LYP/(6-31G**+LANL2DZ) level (see the experimental section for details). The geometries of the complexes were fully optimized and show a similar near-octahedral coordination of the Ir metal to those observed in their X-ray structures. The Ir–C and Ir–N bond distances calculated for the four complexes in the electronic ground state (S_0) are listed in Table 5 together with the experimental X-ray data. The structural trends remarked above from the experimental data are well supported by the theoretical calculations. For instance, the Ir–C1 distance remains constant (2.10 Å) for all complexes, slightly overestimating the experimental value (2.07 Å), and the Ir–C3 distance (~2.06 Å) is always longer than the Ir–C2 distance (~2.02 Å), likely due to the strong *trans* effect induced by the carbene group of the ancillary ligand. The Ir–N1 distance is also predicted to shorten upon the introduction of electron-withdrawing groups on the cyclometallated ligands, but the shortening calculated in passing from **5** to **3** (0.007 Å) is significantly less pronounced than that observed from X-ray data (0.020 Å). Notice that the calculated Ir–N and Ir–C(carbene) distances are overestimated, which is typically observed when using the B3LYP functional.[45]

Table 5 Selected bond distances (in Å) calculated for complexes **3**, **4**, **5**, and **6** in the S_0 singlet ground state and in the T_1 and the metal-centered (^{3}MC) triplet excited states. X-ray values are included for comparison

		Exp. (Table 2)	S_0	T_1	$^3MC_{carbene}$ [a]	$^3MC_{ppy}$
3	Ir–N1	2.149(3)	2.226	2.231		2.216
	Ir–N2	2.054(2)	2.082	2.064	2.075	2.305
	Ir–N3	2.053(2)	2.091	2.097	2.080	2.729
	Ir–C1	2.073(3)	2.100	2.112	2.097	2.042
	Ir–C2	2.006(3)	2.017	2.002	2.046	2.021
	Ir–C3	2.060(3)	2.061	2.058	2.045	2.084
4	Ir–N1	2.153(4)	2.227	2.232		2.223
	Ir–N2	2.058(4)	2.081	2.099	2.083	2.324
	Ir–N3	2.063(4)	2.090	2.067	2.072	2.708
	Ir–C1	2.064(5)	2.101	2.107	2.103	2.045
	Ir–C2	2.010(5)	2.022	2.004	2.045	2.022
	Ir–C3	2.053(5)	2.064	2.062	2.050	2.083
5	Ir–N1	2.169(4)	2.233	2.249		2.252
	Ir–N2	2.056(4)	2.083	2.104	2.081	2.402
	Ir–N3	2.067(4)	2.091	2.074	2.073	2.666
	Ir–C1	2.070(5)	2.100	2.115	2.093	2.056
	Ir–C2	2.027(5)	2.025	1.984	2.046	2.007
	Ir–C3	2.068(5)	2.067	2.061	2.045	2.073
6	Ir–N1	2.143(6)	2.234	2.319		2.242
	Ir–N2	2.055(7)	2.080	2.086	2.069	2.358
	Ir–N3	2.055(7)	2.088	2.078	2.077	2.729
	Ir–C1	2.074(8)	2.103	2.137	2.102	2.049
	Ir–C2	2.037(8)	2.025	1.979	2.044	2.008
	Ir–C3	2.069(7)	2.067	2.027	2.045	2.080

[a] The Ir–N1 distance is not given for the $^3MC_{carbene}$ state because the pyridine ring of the ancillary ligand is decoordinated in this state.

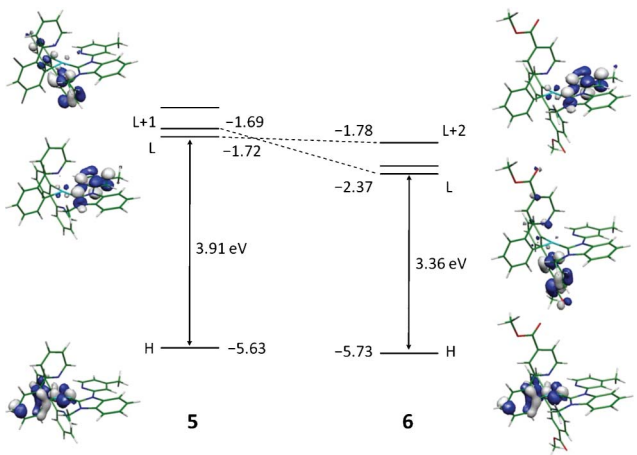

Fig. 5 Schematic diagram showing the electronic density contours (0.05 e.bohr^{-3}) and the energy values (in eV) calculated for the frontier molecular orbitals of complexes **5** and **6**. H and L denote HOMO and LUMO, respectively.

Fig. 5 displays the energy and the atomic orbital composition of the highest-occupied and lowest-unoccupied molecular orbitals (HOMOs and LUMOs) for complexes **5** and **6**. As expected, the HOMO of all complexes is composed of a mixture of Ir d_π orbitals and phenyl π orbitals distributed among the two ppy ligands. Upon the attachment of electron-withdrawing groups such as fluorine (**3** and **4**) and ester groups (**3** and **6**) to the cyclometallated ligands, the HOMO level becomes stabilized following the sequence: **5** (–5.63 eV), **6** (–5.73 eV), **4** (–5.98 eV) and **3** (–6.18 eV), which is in good agreement with the more positive oxidation potentials measured experimentally (**5**: +0.86 V, **6**: +0.94 V, **4**: +1.19 V, **3**: +1.38 V). The HOMO stabilization computed on going from **5** to **3** (0.55 eV) is very close to the increase of the oxidation potential (0.52 V) and is due both to the presence of the fluorine substituents, which stabilizes the HOMO by 0.35 eV as obtained for **4**, and to the attachment of the ester groups. In complex **6** ester groups are attached to the pyridine rings of the main ligand and only remotely influence the orthometallated phenyls where the electron density is located in the HOMO.

Theoretical calculations show that the LUMO of **5** resides on the ancillary ligand showing no overlap with the HOMO (Fig. 5). In contrast, the LUMO+1 and LUMO+2, which are slightly above the LUMO (0.03 and 0.15 eV, respectively), are mainly located on the pyridine rings of the cyclometallated ligands. Similar results are obtained for complex **4**, for which the LUMO is slightly stabilized (–1.84 eV) compared with **5** (–1.72 eV). This stabilization supports the less negative reduction potential measured in passing from **5** (–2.43 V) to **4** (–2.26 V). In contrast to complexes **4** and **5**, the LUMO of complex **6** is located on the main ligand due to the strong stabilization that the attachment of ester groups to the pyridine rings of the main ligands causes on the LUMO+1 and LUMO+2 of **5** (see Fig. 5). The LUMO+2 of complex **6** (–1.78 eV) resides on the ancillary ligand and lies at similar energies to the LUMO level of complex **5** (–1.72 eV) because the ester groups slightly affect the ancillary ligand. The lowering of the LUMO energy (0.65 eV) predicted in passing from **5** to **6** is in perfect agreement with the anodic shift of the first reduction potential (0.62 V) measured experimentally. The LUMO of complex **3** (–1.95 eV) is also located on the main ligand and appears at intermediate energies between the LUMO of **5** (–1.72 eV) and **6** (–2.37 eV) in accordance with the reduction potentials recorded experimentally (Table 3).

The energies calculated for the HOMO and the LUMO indicate a significant reduction of the HOMO–LUMO energy gap along the series **3** (4.24 eV), **4** (4.14 eV), **5** (3.91 eV) and **6** (3.36 eV), in good agreement with the red shift observed along this series in both absorption and emission spectra. However, the atomic orbital composition calculated for the LUMO does not support the fact that emission takes place from the main ligand, as experiment suggests, since, depending on the complex, the LUMO is located on the ancillary ligand (**4** and **5**) or on the main ligands (**3** and **6**). As the simple description of the HOMO and LUMO is not always representative of the emitting triplet state, the low-lying triplet states of complexes **3**, **4**, **5** and **6** were calculated using the time-dependent DFT (TD-DFT) as a first approach to further investigate the nature of the emitting excited state. Table 6 summarizes the characteristics of the lowest triplet states computed for these complexes at the optimized geometry of the ground state (S_0).

TD-DFT calculations predict that the lowest-energy triplet state (T_1) shows a similar nature for the four complexes (Table 6). It is described as a mixture of metal-to-ligand charge transfer (MLCT) and ligand-centered (LC) character since the monoelectronic excitations that define T_1 involve the HOMO and HOMO–1, which are mixtures of Ir d_π orbitals and ppy π orbitals, and the LUMO of the cyclometallated ligand, that corresponds to the LUMO in **3** and **6** and to the LUMO+1 in **4** and **5**. The first excited triplet implying the N^C: ancillary ligand (T_3 for **3**, **4** and **5** and T_5 for **6**) is well separated (0.3–0.7 eV) from T_1. TD-DFT calculations therefore suggest that the lowest-energy triplet of this series of compounds mainly involves the cyclometallated ligand

Table 6 Lowest triplet excited states calculated at the B3LYP(6-31G**+LANL2DZ) level for complexes **3**, **4**, **5** and **6**. Vertical excitation energies (*E*), dominant monoexcitations with contributions (within parentheses) greater than 0.30, nature of the electronic transition and description of the excited state are summarized

		E (eV)	Monoexcitations	Nature	Description[a]
3	T_1	2.96	H–1 → L (0.32) H → L (0.39)	$d_\pi(Ir) + \pi_{ppy} \rightarrow \pi^*_{ppy}$	^{3}MLCT/^{3}LC
	T_2	3.00	H → L+2 (0.42)	$d_\pi(Ir) + \pi_{ppy} \rightarrow \pi^*_{ppy}$	^{3}MLCT/^{3}LC
	T_3	3.43	H → L+1 (0.37) H–2 → L+1 (0.32)	$d_\pi(Ir) + \pi_{ppy} \rightarrow \pi^*_{carbene}$	^{3}MLCT/^{3}LLCT
4	T_1	2.91	H–1 → L+1 (0.39) H → L+1 (0.39)	$d_\pi(Ir) + \pi_{ppy} \rightarrow \pi^*_{ppy}$	^{3}MLCT/^{3}LC
	T_2	2.95	H → L+2 (0.45)	$d_\pi(Ir) + \pi_{ppy} \rightarrow \pi^*_{ppy}$	^{3}MLCT/^{3}LC
	T_3	3.33	H → L (0.51)	$d_\pi(Ir) + \pi_{ppy} \rightarrow \pi^*_{carbene}$	^{3}MLCT/^{3}LLCT
5	T_1	2.80	H → L+1 (0.52)	$d_\pi(Ir) + \pi_{ppy} \rightarrow \pi^*_{ppy}$	^{3}MLCT/^{3}LC
	T_2	2.84	H → L+2 (0.52)	$d_\pi(Ir) + \pi_{ppy} \rightarrow \pi^*_{ppy}$	^{3}MLCT/^{3}LC
	T_3	3.09	H → L (0.66)	$d_\pi(Ir) + \pi_{ppy} \rightarrow \pi^*_{carbene}$	^{3}MLCT/^{3}LLCT
6	T_1	2.48	H → L (0.61)	$d_\pi(Ir) + \pi_{ppy} \rightarrow \pi^*_{ppy}$	^{3}MLCT/^{3}LC
	T_2	2.51	H → L+1 (0.62)	$d_\pi(Ir) + \pi_{ppy} \rightarrow \pi^*_{ppy}$	^{3}MLCT/^{3}LC
	T_3	2.85	H–1 → L (0.42) H → L (0.31)	$d_\pi(Ir) + \pi_{ppy} \rightarrow \pi^*_{ppy}$ $d_\pi(Ir) + \pi_{ppy} \rightarrow \pi^*_{ppy}$	^{3}MLCT/^{3}LC
	T_5	3.14	H → L+2 (0.46)	$d_\pi(Ir) + \pi_{ppy} \rightarrow \pi^*_{carbene}$	^{3}MLCT/^{3}LLCT

[a] MLCT, LC and LLCT denote metal-to-ligand charge transfer, ligand-centered and ligand-to-ligand charge transfer, respectively.

and the Ir metal core, in contrast to what is found for complexes bearing N^N ancillary ligands.[10,22,36]

To further investigate the nature of the lowest-energy triplet state, the geometry of this state was optimized using the spin-unrestricted DFT approach. After full-geometry relaxation, the T_1 state defined by the TD-DFT calculations continues to be the most stable triplet for the four complexes. The spin density calculated for the optimized T_1 state indicates that excitation to T_1 implies an electron promotion from the Ir-ppy environment to the cyclometallated ligands. This is illustrated in Fig. 6 for complexes **4**, **5** and **6**, for which the unpaired-electron spin density distribution perfectly matches the topology of the monoelectronic excitations in which the T_1 state originates (HOMO → LUMO for **3** and **6**, and HOMO → LUMO+1 for **4** and **5**). The electron promotion

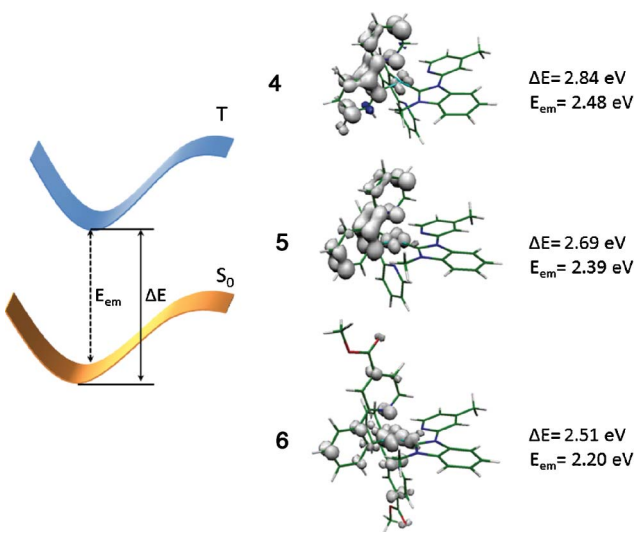

Fig. 6 Schematic energy diagram showing the adiabatic energy difference (ΔE) between S_0 and T_1 and the emission energy (E_{em}) from T_1 calculated for complexes **4**, **5** and **6**. The unpaired-electron spin-density contours (0.005 e.bohr^{-3}) computed for the optimized T_1 state are also shown.

associated with the excitation to T_1 causes small changes (0.01–0.02 Å) in the coordination sphere of the complex (Table 5). T_1 is computed to lie 2.84 (**3**), 2.84 (**4**), 2.69 (**5**) and 2.51 eV (**6**) above S_0 (adiabatic energy differences, ΔE in Fig. 6).

The nature of the T_1 state can therefore be described as a mixed ^{3}MLCT/^{3}LC state with no participation of the N^C: ancillary ligand (see Fig. 6). The calculated spin densities show an increase of the metal contribution (MLCT character) on going from **3** to **6** (Ir: 0.10, ligand: 1.90 for **3**; Ir: 0.37, ligand: 1.63 for **4**; Ir: 0.38, ligand: 1.62 for **5**; and Ir: 0.45, ligand: 1.55 for **6**) as anticipated from the photophysical results. The large LC character of the emitting state explains the structured aspect of the emission band observed for complexes **3**, **4** and **5** (Fig. 4). To estimate the phosphorescence emission energy, the vertical energy difference between T_1 and S_0 was computed by performing a single-point calculation of S_0 at the optimized minimum-energy geometry of T_1 (Fig. 6). Calculations lead to vertical emission energies of 2.46 eV for **3**, 2.48 eV for **4**, 2.39 eV for **5** and 2.20 eV for **6**, in reasonably good agreement with the experimental values for the maximum emission (Table 3).

One of the most important deactivation pathways of the phosphorescent emission from T_1 in transition-metal complexes is the population of the metal-centered (^{3}MC) triplet excited states.[43,46–49] Metal-centered states result from the excitation of an electron from the occupied t_{2g} (dπ) HOMO to the unoccupied e_g (dσ*) orbitals of the metal. As sketched in Fig. 7, dσ* orbitals involve σ-antibonding interactions between the iridium core and the nitrogen atoms of either the ancillary or the cyclometallated ligands. Two different types of ^{3}MC states, here named $^3MC_{carbene}$ and $^3MC_{ppy}$, result from these interactions which involve the decoordination of one ($^3MC_{carbene}$) and two ($^3MC_{ppy}$) Ir–N bonds leading to five- and four-coordinated structures in the excited state, respectively.

The geometries of both ^{3}MC states ($^3MC_{ppy}$ and $^3MC_{carbene}$) were fully relaxed starting from the optimised geometry of S_0 and lengthening the respective Ir–N bond distances to 2.70 Å. Similar optimized structures were obtained for the four complexes (see

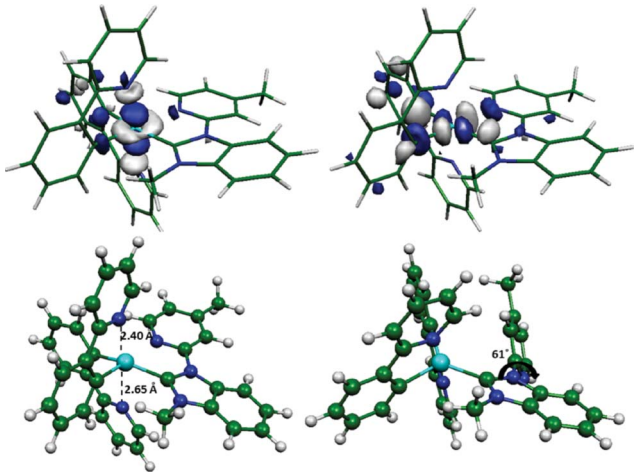

Fig. 7 Top: Electron density contours (0.04 e bohr^{-3}) calculated for the unoccupied e_g molecular orbitals of **5** showing σ-antibonding interactions along the vertical N_{ppy}–Ir–N_{ppy} axis (left) and with the N^C: ancillary ligand (right). Bottom: Minimum-energy structures calculated for the $^3MC_{ppy}$ (left) and $^3MC_{carbene}$ (right) states of **5**.

Table 5). As expected, the most important structural change found for the $^3MC_{ppy}$ state concerns the Ir–N_{ppy} bonds, whose values lengthen by 0.3–0.7 Å compared to S_0 and range between 2.35 and 2.75 Å. For the $^3MC_{carbene}$ state, the pyridine ring of the ancillary ligand twists around the inter-ring bond by 60–75° and the nitrogen atom is fully decoordinated (see Fig. 7 bottom). The molecular structures calculated for both ^3MC states are in good agreement with those obtained for similar iridium(III) complexes.[14,44] The rupture of the metal–ligand bonds and, consequently, the opening of the coordination sphere enhances the reactivity of the complex and facilitates its degradation. The spin densities calculated for the $^3MC_{ppy}$ and $^3MC_{carbene}$ states (Fig. 8) reflect the σ-interactions that characterize these states and corroborate their metal-centered character.

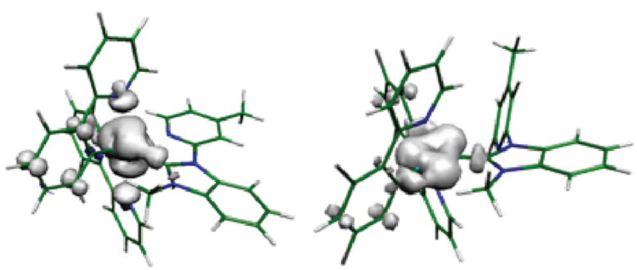

Fig. 8 Unpaired-electron spin-density contours (0.005 e bohr^{-3}) calculated for the $^3MC_{ppy}$ (left) and $^3MC_{carbene}$ (right) states of **5**.

More relevant than the molecular structure is the relative energy position of the ^3MC states with respect to the emitting triplet state. After geometry relaxation, the $^3MC_{carbene}$ state is calculated to lie below the T_1 state (0.2–0.3 eV for **3**, **4** and **5** and only 5×10^{-4} eV for **6**), while the $^3MC_{ppy}$ state is located above the emitting state (~0.10 eV for **3**, **4** and **5** and 0.87 eV for **6**). Therefore, calculations suggest that both ^3MC states could be thermally populated and play a role in the deactivation of the emission process. This would explain the poor photophysical properties obtained in this series of compounds. However, the theoretical data only concerns the relative adiabatic position of the ^3MC states with respect to T_1 and additional experimental studies, such as temperature-dependent analysis of the emitting excited-state lifetime, are needed to evaluate the activation energy barriers for populating the ^3MC states. Progress in this direction is underway.

Electroluminescent properties

Finally we performed initial tests of complexes **4** (blue), **5** (green) and **6** (red) in simple devices as required colors for white. LEC devices incorporating the carbene-based complex materials were fabricated *via* spin-coating under ambient conditions on patterned indium tin oxide (ITO)-covered glass substrates. Prior to the deposition of the emitting layer a 100 nm layer of poly-(3,4-ethylenedioxythiophene)-poly-(styrenesulfonate) PEDOT:PSS was deposited to planarize the ITO anode, increasing the yield and reproducibility of working devices. The emitting layer was prepared by dissolving six percent by weight of the corresponding complex and the ionic liquid (IL) 1-butyl-3-methylimidazolium hexafluorophosphate [BMIM][PF_6] in a molar ratio of 3 : 1 in 0.5 mL of acetonitrile. [BMIM][PF_6] was used to enhance the ionic conductivity of the active layer accompanied with a reduction of the turn-on time of the device.[17] The solutions were filtered using a 0.1 μm PTFE-filter and spin-coated on top of the PEDOT : PSS layer. Afterwards, the substrate was transferred to a nitrogen filled glovebox (O_2 and H_2O < 1 ppm) and annealed on a hotplate at 100 °C for 1 h resulting in an emitting layer thickness of 150 nm. Finally, a 150 nm thick aluminum (Al) cathode was thermally evaporated on top under high vacuum (<10^{-6} mbar) using a shadow mask, defining 8 pixels per substrate, each having an active lighting area of 4 mm^2. The device was encapsulated by a glass capping layer to protect the organic layers against penetrating oxygen and water.

Fig. 9 displays the electroluminescent spectra measured for complexes **4**, **5** and **6** at a fixed voltage of 8 V. The spectra were recorded immediately after emission could be observed. The

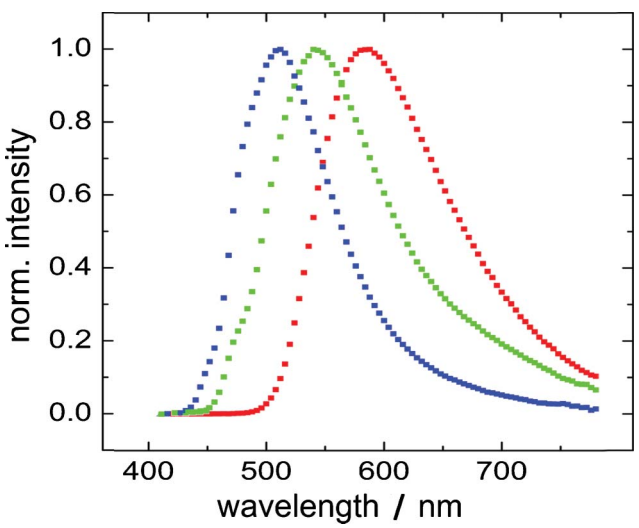

Fig. 9 Normalized electroluminescence spectra of the LEC devices incorporating the **4** (blue), **5** (green) and **6** (red) emitter at a constant voltage of 8 V immediately after emission could be observed.

devices with **4** and **5** exhibit green electroluminescence with a maximum located at around 512 and 544 nm, respectively, whereas for the device with **6** an orange emission is observed with an electroluminescence maximum at around 584 nm.

Upon applying a bias to the LEC devices, light emission slowly increases in intensity with time. The emission is characterized by a slow increase of both current density and luminance, due to the slow movement of the counter-anions to the interfaces of the electrodes which assists in the charge injection process as described for LECs based on ruthenium and iridium complexes.[1] In our devices, the luminance values are very different for the three complexes. Devices with **4** and **5** present a low luminance and efficiency values at around 20 cd m^{-2} and 10^{-3} cd A^{-1} at 6 V, while the device with **6** is very bright (1070 cd m^{-2}) and efficient 4.7 cd A^{-1} at the same voltage. Additionally, the electroluminescence spectra observed for complexes **4** and **5** are strongly red-shifted with respect to the PL spectra obtained in solution (Fig. 4 and 9). This behavior has already been observed in other LEC devices and should be ascribed to either a polarization effect due to electrical excitation or a change of emissive excited state in solid-state.[6,7,50] Ongoing accurately photophysical and device studies are being carried out to unveil the underlying reason of both the low performance level and the red-shift EL emission observed in LECs with **4** and **5**.

Conclusions

In conclusion, we have developed a new family of electroactive charged bis-cyclometallated iridium(III) complexes based on pyridine-carbene as neutral ancillary ligand that emit from near-UV to red. This design holds great promise for developing deep-blue- and deep-red-emitting charged iridium complexes suitable for LECs applications. This is due to the emitting excited state being localized on the main C^N ligands, which therefore control the emitting properties of the complex. This represents a paradigmatic shift from usual charged complexes based on N^N ancillary ligands forming a five-membered ring with the central metal cation, where the emission properties are largely controlled by the ancillary ligand.

Experimental procedures

Materials and methods

Iridium trichloride hydrate was purchased from Heraeus. All solvents were used as pa grade and degassed by three consecutive vacuum and back-fill cycles. 3-Methyl-1-(4-methyl-2-pyridyl)benzimidazolium iodide (pmbi),[34,35] 2′,6′-difluoro-2,3′-bipyridine[51] and $[Ir(C^N)_2(\mu\text{-}Cl)]_2$ [10,52,53] were prepared according to literature procedures. All other materials and solvents were of reagent quality and used as received. ^1H and ^{13}C NMR spectra were recorded using a Bruker AV 400 MHz spectrometer. Chemical shifts δ (in ppm) are referenced to residual solvent peaks. For ^1H NMR: $CDCl_3$, 7.24 ppm; for ^{13}C NMR: $CDCl_3$, 77.0 ppm. ^{19}F and ^{31}P NMR were recorded using a Bruker AV 200 MHz spectrometer. Coupling constants are expressed in hertz (Hz). High-resolution mass spectra (HRMS) were obtained with a Waters Q-TOF-MS instrument using electrospray ionisation (ESI). UV-visible spectra were recorded in a 1 cm path length quartz cell on a Cary 100 spectrophotometer. Emission spectra were recorded on a Fluorolog 3–22 using a 90° optical geometry. The photoluminescence quantum yields were determined using quinine sulfate (10^{-5} M in 1 N H_2SO_4; air equilibrated; Φ_L = 0.546) and $[Ru(bpy)_3][PF_6]_2$ (10^{-5} M in water; air equilibrated; Φ_L = 0.028) as standards. Excited-state lifetimes were measured using a FL-1061PC TCSPC and 371 and 406 nm Nanoled as excitation source. Voltammetric measurements employed a PC controlled AutoLab PSTAT10 electrochemical workstation and were carried out in an Ar-filled glove box, oxygen and water < 1 ppm. Cyclic Voltammetry (CV) and Differential Pulse Voltammetry (DPV) techniques were used to estimate the redox potentials. DPV was used in support for CV to obtain a better estimate of the electrochemical potentials when the systems show behavior near to the irreversibility, *i.e.* one of the two peaks in the CV is not well defined. DPVs were carried out sweeping from negative to positive potentials and mean values are calculated. CVs were obtained at a scan rate of 1 and 0.1 $V.s^{-1}$. DPVs were obtained at a Modulation Potential of 50 mV, a Step Potential of 10 mV, a Modulation Time of 50 ms and an Interval Time of 100 ms. Measurements were carried out using 0.1 M $TBAPF_6$ as supporting electrolyte in acetonitrile (MeCN). Glassy carbon, platinum plate and platinum wire were used as working, counter and quasi-reference electrodes, respectively. At the end of each measurement, ferrocene was added as an internal reference. Data collections for X-ray crystal structures were performed at low temperature [100(2) K] using Mo-Kα radiation on a Bruker APEX II CCD, having kappa geometry. All data sets were reduced by means of EvalCCD[54] and then corrected for absorption.[55] The solutions and refinements were performed by SHELX.[56] The crystal structures were refined using full-matrix least-squares based on F^2 with all non hydrogen atoms anisotropically defined. Hydrogen atoms were placed in calculated positions by means of the "riding" model.

Computational details

Density Functional Theory (DFT) calculations were carried out with the D.02 revision of the Gaussian 03 program package,[57] using Becke's three-parameter B3LYP exchange-correlation functional[58,59] together with the 6-31G** basis set for C, H, O, F and N atoms[60] and the "double-ζ" quality LANL2DZ basis set for the Ir element.[61] An effective core potential (ECP) replaces the inner core electrons of Ir leaving the outer core $[(5s)^2(5p)^6]$ electrons and the $(5d)^6$ valence electrons of Ir(III). The geometries of the singlet ground state (S_0) and of the lowest triplet excited state (T_1) were fully optimized. Triplet states were calculated at the spin-unrestricted UB3LYP level with a spin multiplicity of 3. The expected values calculated for S^2 were always smaller than 2.05. Solvent effects were considered within the SCRF (self-consistent reaction field) theory using the polarized continuum model (PCM) approach to model the interaction with the solvent.[62,63] Molecular orbitals were calculated in acetonitrile using gas-phase optimized geometries. Starting from the closed-shell S_0 state, time-dependent DFT (TD-DFT) calculations[64–66] were performed in acetonitrile solution to determine the energies and the electronic nature of the lowest excited triplet states at the ground-state geometry. Vertical electronic excitation energies were determined for the lowest 10 triplet states.

General procedure for the preparation of Ir carbene complexes

A solution of 74 mg (0.21 mmol, 2.1 eq) of 3-methyl-1-(4-methyl-2-pyridyl)benzimidazolium iodide, 28 mg (0.12 mmol, 1.2 eq) of silver(I) oxide, and 0.10 mmol (0.5 eq) of the corresponding iridium dimer in 12 mL of 1,2-dichloroethane was degassed (3 vacuum and back-fill cycles) and heated to reflux (95 °C) overnight. After cooling to ambient temperature, the mixture was filtered through celite to remove silver residues. The celite was washed with CH_2Cl_2 and the solvent was removed in vacuo. The residue was redissolved in 20 mL of CH_2Cl_2 and extracted three times with an aqueous KPF_6 solution (55 mg of KPF_6 in 40 mL of water per cycle). The combined organic layers were washed with water, dried over $MgSO_4$ and concentrated in vacuo. The crude product was purified by column chromatography on silica gel using CH_2Cl_2, and then CH_2Cl_2/acetone (p.a. grade) 4/1 as solvent. After evaporation of the solvent the pure product was obtained.

[(1-(2,4-difluorophenyl)-1*H*-pyrazole)$_2$Ir(pmbi)]PF$_6$ 1

Off-white solid. Yield: 125 mg (0.135 mmol, 68%). ^{1}H NMR (400 MHz, $CDCl_3$): δ 8.33 (dd, $^3J_{HH}$ = 9.3 Hz, $^4J_{HH}$ = 2.7 Hz, 2H, ArH), 8.28 (d, $^3J_{HH}$ = 8.3 Hz, 1H, ArH), 8.26 (s, 1H, ArH), 7.74 (d, $^3J_{HH}$ = 5.7 Hz, 1H, ArH), 7.62–7.58 (m, 1H, ArH), 7.48 (d, $^3J_{HH}$ = 4.2 Hz, 2H, ArH), 7.16 (br, 1H, ArH), 7.09 (d, $^3J_{HH}$ = 5.8 Hz, 1H, ArH), 6.95 (br, 1H, ArH), 6.70–6.61 (m, 2H, ArH), 6.51 (bt, $^4J_{HH}$ = 2.6 Hz, 1H, ArH), 5.73 (bt, $^3J_{HH}$ = 7.1 Hz, 1H, ArH), 3.53 (s, 3H, NCH_3), 2.71 (s, 3H, CH_3). ^{31}P NMR (81 MHz, $CDCl_3$): δ –144.6 (sept, $^1J_{PF}$ = 713 Hz, PF_6). ^{19}F NMR (188 MHz, $CDCl_3$): δ –73.3 (d, $^1J_{PF}$ = 712 Hz, PF_6), –111.1 (m, ArF), –111.6 (m, ArF), –123.5 (vq, J = 5.8 Hz, ArF), –123.6 (vq, J = 5.7 Hz, ArF). HRMS (ESI-TOF) m/z (%): calcd. 774.1580; found 774.1582 (100) [(M–PF_6)$^+$].

[(2′,6′-difluoro-2,3′-bipyridine)$_2$Ir(pmbi)]PF$_6$ 2

Pale yellow solid. Yield: 106 mg (0.112 mmol, 56%). ^{1}H NMR (400 MHz, acetone-D_6): δ 8.65–8.59 (m, 3H, ArH), 8.44–8.41 (m, 2H, ArH), 8.14 (q, $^3J_{HH}$ = 8.2 Hz, 2H, ArH), 8.05–8.01 (m, 2H, ArH), 7.82–7.80 (m, 1H, ArH), 7.65–7.61 (m, 2H, ArH), 7.38 (d, $^3J_{HH}$ = 5.8 Hz, 1H, ArH), 7.28 (td, $^3J_{HH}$ = 6.7 Hz, $^4J_{HH}$ = 1.3 Hz, 1H, ArH), 7.24 (td, $^3J_{HH}$ = 6.7 Hz, $^4J_{HH}$ = 1.3 Hz, 1H, ArH), 6.01 (t, $^4J_{HH}$ = 1.9 Hz, 1H, ArH), 3.78 (t, $^4J_{HH}$ = 2.4 Hz, 1H, ArH), 3.71 (s, 3H, NCH_3), 2.72 (s, 3H, CH_3). ^{31}P NMR (81 MHz, acetone-D_6): δ –144.3 (sept, $^1J_{PF}$ = 707 Hz, PF_6). ^{19}F NMR (188 MHz, acetone-D_6): δ –68.9 (dd, J = 40.3, 8.8 Hz, ArF), –71.2 (dd, J = 190.4, 9.5 Hz, ArF), –72.6 (d, $^1J_{PF}$ = 706 Hz, PF_6). HRMS (ESI-TOF) m/z (%): calcd. 798.1582; found 798.1462 (100) [(M–PF_6)$^+$].

[(Methyl 2,6-difluoro-3-(pyridin-2-yl) benzoate)$_2$Ir(pmbi)]PF$_6$ 3

Yellow solid. Yield: 106 mg (0.10 mmol, 50%). ^{1}H NMR (400 MHz, $CDCl_3$): δ 8.36–8.32 (m, 2H, ArH), 8.28–8.26 (m, 2H, ArH), 7.99 (dd, $^3J_{HH}$ = 5.8 Hz, $^4J_{HH}$ = 1.0 Hz, 1H, ArH), 7.86–7.81 (m, 2H, ArH), 7.63 (dd, $^3J_{HH}$ = 5.9 Hz, $^4J_{HH}$ = 0.8 Hz, 1H, ArH), 7.58–7.51 (m, 2H, ArH), 7.46–7.42 (m, 2H, ArH), 7.18–7.07 (m, 3H, ArH), 5.86 (d, $^3J_{HH}$ = 9.6 Hz, 1H, ArH), 5.63 (d, $^3J_{HH}$ = 8.6 Hz, 1H, ArH), 3.91 (s, 3H, OCH_3), 3.89 (s, 3H, OCH_3), 3.45 (s, 3H, NCH_3), 2.66 (s, 3H, CH_3). ^{31}P NMR (81 MHz, $CDCl_3$): δ –144.7 (sept, $^1J_{PF}$ = 713 Hz, PF_6). ^{19}F NMR (188 MHz, $CDCl_3$): δ –73.2 (d, $^1J_{PF}$ = 712 Hz, PF_6), –105.7 (vt, J = 7.1 Hz, ArF), –106.0 (vt, J = 8.2 Hz, ArF), –109.9 (br, 2ArF). HRMS (ESI-TOF) m/z (%): calcd. 912.1785; found 912.1788 (100) [(M–PF_6)$^+$].

[(2-(2,4-difluorophenyl)pyridine)$_2$Ir(pmbi)]PF$_6$ 4

Yellow solid. Yield: 93 mg (0.10 mmol, 50%). ^{1}H NMR (400 MHz, $CDCl_3$): δ 8.30 (d, $^3J_{HH}$ = 8.0 Hz, 3H, ArH), 8.27 (s, 1H, ArH), 7.95 (bd, $^3J_{HH}$ = 5.8 Hz, 1H, ArH), 7.81–7.76 (m, 2H, ArH), 7.61–7.57 (m, 3H, ArH), 7.47–7.42 (m, 2H, ArH), 7.12–7.02 (m, 3H, ArH), 6.60–6.48 (m, 2H, ArH), 5.79 (dd $^3J_{HH}$ = 8.6 Hz, $^4J_{HH}$ = 2.3 Hz, 1H, ArH), 5.58 (dd, $^3J_{HH}$ = 7.7 Hz, $^4J_{HH}$ = 2.3 Hz, 1H, ArH), 3.43 (s, 3H, NCH_3), 2.68 (s, 3H, CH_3). ^{31}P NMR (81 MHz, $CDCl_3$): δ –144.6 (sept, $^1J_{PF}$ = 713 Hz, PF_6). ^{19}F NMR (188 MHz, $CDCl_3$): δ –73.3 (d, $^1J_{PF}$ = 712 Hz, PF_6), –105.3 (vq, J = 9.1 Hz, ArF), –105.7 (vq, J = 9.5 Hz, ArF), –108.0 (vt, J = 11.8 Hz, ArF), –108.6 (vt, J = 11.7 Hz, ArF). HRMS (ESI-TOF) m/z (%): calcd. 796.1675; found 796.1677 (100) [(M–PF_6)$^+$].

[(2-phenylpyridine)$_2$Ir(pmbi)]PF$_6$ 5

Yellow solid. Yield: 165 mg (0.19 mmol, 95%). ^{1}H NMR (400 MHz, $CDCl_3$): δ 8.29 (d, $^3J_{HH}$ = 8.4 Hz, 1H, ArH), 8.23 (s, 1H, ArH), 7.95 (bd, $^3J_{HH}$ = 5.1 Hz, 1H, ArH), 7.90 (bt, $^3J_{HH}$ = 6.8 Hz, 2H, ArH), 7.76–7.71 (m, 2H, ArH), 7.68 (bt, $^3J_{HH}$ = 6.9 Hz, 2H, ArH), 7.60 (bd, $^3J_{HH}$ = 5.7 Hz, 1H, ArH), 7.57 (bt, $^3J_{HH}$ = 7.7 Hz, 2H, ArH), 7.45–7.39 (m, 2H, ArH), 7.06–6.94 (m, 6H, ArH), 6.86 (dt, $^3J_{HH}$ = 5.0 Hz, $^4J_{HH}$ = 1.3 Hz, 1H, ArH), 6.40 (dd, $^3J_{HH}$ = 7.6 Hz, $^4J_{HH}$ = 0.9 Hz, 1H, ArH), 6.18 (dd, $^3J_{HH}$ = 7.3 Hz, $^4J_{HH}$ = 1.0 Hz, 1H, ArH), 3.35 (s, 3H, NCH_3), 2.66 (s, 3H, CH_3). ^{31}P NMR (81 MHz, $CDCl_3$): δ –144.5 (sept, $^1J_{PF}$ = 713 Hz, PF_6). ^{19}F NMR (188 MHz, $CDCl_3$): δ –73.4 (d, $^1J_{PF}$ = 712 Hz, PF_6). HRMS (ESI-TOF) m/z (%): calcd. 724.2052; found 724.2054 (100) [(M–PF_6)$^+$].

[(Methyl 2-phenylisonicotinate)$_2$Ir(pmbi)] PF$_6$ 6

Orange solid. Yield: 167 mg (0.17 mmol, 85%). ^{1}H NMR (400 MHz, $CDCl_3$): δ 8.44 (d, $^3J_{HH}$ = 14.7 Hz, 2H, ArH), 8.25 (d, $^3J_{HH}$ = 8.3 Hz, 1H, ArH), 8.22 (s, 1H, ArH), 8.15 (d, $^3J_{HH}$ = 6.0 Hz, 1H, ArH), 7.79 (bt, $^3J_{HH}$ = 6.8 Hz, 3H, ArH), 7.52–7.49 (m, 4H, ArH), 7.41 (bt, $^3J_{HH}$ = 8.3 Hz, 2H, ArH), 7.08 (bt, $^3J_{HH}$ = 7.6 Hz, 1H, ArH), 6.98 (m, 3H, ArH), 6.89 (bt, $^3J_{HH}$ = 7.3 Hz, 1H, ArH), 6.38 (d, $^3J_{HH}$ = 7.6 Hz, 1H, ArH), 6.15 (d, $^3J_{HH}$ = 7.4 Hz, 1H, ArH), 3.94 (s, 6H, OCH_3), 3.33 (s, 3H, NCH_3), 2.63 (s, 3H, CH_3). ^{13}C NMR (100 MHz, $CDCl_3$): δ 187.1 (NCN), 169.7 (COOMe), 168.3 (COOMe), 164.5, 164.4, 163.9, 153.4, 154.1, 154.0, 149.6, 149.5, 149.4, 143.2, 141.8, 138.9, 138.3, 136.3,131.7, 131.4, 131.2, 131.1, 130.8, 126.1, 125.5, 125.5, 125.0, 123.6, 123.5, 122.4, 122.2, 119.6, 119.2, 114.4, 113.1, 111.8 (ArC), 53.2 (OMe), 53.1 (OMe), 33.7 (NMe), 21.9 (Me). ^{31}P NMR (81 MHz, CDCl3): δ –144.6 (sept, $^1J_{PF}$ = 713 Hz, PF_6). ^{19}F NMR (188 MHz, $CDCl_3$): δ –73.3 (d, $^1J_{PF}$ = 712 Hz, PF_6). HRMS (ESI-TOF) m/z (%): calcd. 840.2162; found 840.2164 (100) [(M–PF_6)$^+$].

[(Methyl 2-(phenanthren-9-yl)isonicotinate)$_2$Ir(pmbi)]PF$_6$ 7

Red solid. Yield: 130 mg (0.11 mmol, 55%). ^{1}H NMR (400 MHz, $CDCl_3$): δ 8.85 (s, 1H, ArH), 8.79 (s, 1H, ArH), 8.52–8.36 (m, 6H, ArH), 8.15–8.11 (m, 2H, ArH), 8.05 (d, $^3J_{HH}$ = 6.1 Hz, 1H, ArH), 7.75–7.70 (m, 2H, ArH), 7.64–7.58 (m, 2H, ArH), 7.52–7.48 (m, 4H, ArH), 7.43–7.30 (m, 6H, ArH), 6.91–6.76 (m, 3H,

ArH), 5.58–5.52 (m, 1H, ArH), 3.92 (br, 6H, OCH_3), 3.06 (s, 3H, NCH_3), 2.66 (s, 3H, CH_3). ^{31}P NMR (81 MHz, $CDCl_3$): δ −144.6 (sept, $^1J_{PF}$ = 713 Hz, PF_6). ^{19}F NMR (188 MHz, $CDCl_3$): δ −73.2 (d, $^1J_{PF}$ = 712 Hz, PF_6). HRMS (ESI-TOF) m/z (%): calcd. 1040.2788; found 1040.2793 (100) [$(M–PF_6)^+$].

Device preparation and characterization

Poly-(3,4-ethylenedioxythiophene)-poly-(styrenesulfonate) aqueous dispersion (PEDOT:PSS) (CleviosTM P VP AI4083) was purchased from Heraeus (formerly H. C. Starck). Acetonitrile (anhydrous, 99.8%) and 1-butyl-3-methyl-imidazolium hexafluorophosphate [BMIM][PF_6] (purum, ≥97.0%) were obtained from Sigma Aldrich and were used as received. Indium tin oxide (ITO)-coated glass plates were patterned using conventional photolithography. Before deposition of the organic layers, the substrates were extensively cleaned using sonification in detergent bathes and subsequent oxygen plasma treatment. The thicknesses of the films were determined using a KLA Tencor P·15 profilometer. The electro-optical characterization was carried out in a Botest OLED Lifetime Test System (OLT) under a constant voltage operation of 8 V at a constant temperature of 20 °C. Using a Photo Research PR–650 SpectraScan® Colorimeter the photodiodes were calibrated and the electroluminescent spectra of the different LEC devices were detected in the visible range between 380 and 780 nm.

Acknowledgements

This work has been supported by the European Union (CELLO, STRP 248043), the Spanish Ministry of Science and Innovation (MICINN) (MAT2007-61584, CSD2007-00010, and CTQ2009-08790). R.D.C. acknowledges the support of the MICINN and the Alexander von Humboldt Foundation.

Notes and references

1 J. D. Slinker, J. Rivnay, J. S. Moskowitz, J. B. Parker, S. Bernhard, H. D. Abruna and G. G. Malliaras, *J. Mater. Chem.*, 2007, **17**, 2976.
2 J. Slinker, D. Bernards, P. L. Houston, H. D. Abruna, S. Bernhard and G. G. Malliaras, *Chem. Commun.*, 2003, 2392.
3 H. J. Bolink, E. Coronado, R. D. Costa, E. Ortí, M. Sessolo, S. Graber, K. Doyle, M. Neuburger, C. E. Housecroft and E. C. Constable, *Adv. Mater.*, 2008, **20**, 3910.
4 S. Graber, K. Doyle, M. Neuburger, C. E. Housecroft, E. C. Constable, R. D. Costa, E. Ortí, D. Repetto and H. J. Bolink, *J. Am. Chem. Soc.*, 2008, **130**, 14944.
5 R. D. Costa, E. Ortí, H. J. Bolink, S. Graber, C. E. Housecroft and E. C. Constable, *J. Am. Chem. Soc.*, 2010, **132**, 5978.
6 H. J. Bolink, L. Cappelli, S. Cheylan, E. Coronado, R. D. Costa, N. Lardies, M. K. Nazeeruddin and E. Ortí, *J. Mater. Chem.*, 2007, **17**, 5032.
7 L. He, L. Duan, J. Qiao, R. J. Wang, P. Wei, L. D. Wang and Y. Qiu, *Adv. Funct. Mater.*, 2008, **18**, 2123.
8 L. He, J. Qiao, L. Duan, G. F. Dong, D. Q. Zhang, L. D. Wang and Y. Qiu, *Adv. Funct. Mater.*, 2009, **19**, 2950.
9 M. Mydlak, C. Bizzarri, D. Hartmann, W. Sarfert, G. Schmid and L. De Cola, *Adv. Funct. Mater.*, 2010, **20**, 1812.
10 A. B. Tamayo, S. Garon, T. Sajoto, P. I. Djurovich, I. M. Tsyba, R. Bau and M. E. Thompson, *Inorg. Chem.*, 2005, **44**, 8723.
11 C.-H. Yang, J. Beltran, V. Lemaur, J. Cornil, D. Hartmann, W. Sarfert, R. Frohlicj, C. Bizzarri and L. De Cola, *Inorg. Chem.*, 2010, **49**, 9891.
12 E. Baranoff, J. H. Yum, M. Graetzel and M. K. Nazeeruddin, *J. Organomet. Chem.*, 2009, **694**, 2661.
13 M. S. Lowry, W. R. Hudson, R. A. Pascal and S. Bernhard, *J. Am. Chem. Soc.*, 2004, **126**, 14129.
14 R. D. Costa, F. J. Céspedes-Guirao, E. Ortí, H. J. Bolink, J. Gierschner, F. Fernández-Lazaro and A. Sastre-Santos, *Chem. Commun.*, 2009, 3886.
15 E. Baranoff, I. Jung, R. Scopelliti, E. Solari, M. Grätzel and M. K. Nazeeruddin, *Dalton Trans.*, 2011, **40**, 6860.
16 Q. Zhao, M. X. Yu, L. X. Shi, S. J. Liu, C. Y. Li, M. Shi, Z. G. Zhou, C. H. Huang and F. Y. Li, *Organometallics*, 2010, **29**, 1085.
17 S. T. Parker, J. D. Slinker, M. S. Lowry, M. P. Cox, S. Bernhard and G. G. Malliaras, *Chem. Mater.*, 2005, **17**, 3187.
18 B. Beyer, C. Ulbricht, D. Escudero, C. Friebe, A. Winter, L. González and U. S. Schubert, *Organometallics*, 2009, **28**, 5478.
19 J. D. Slinker, C. Y. Koh, G. G. Malliaras, M. S. Lowry and S. Bernhard, *Appl. Phys. Lett.*, 2005, **86**, 173506.
20 C. Rothe, C. J. Chiang, V. Jankus, K. Abdullah, X. S. Zeng, R. Jitchati, A. S. Batsanov, M. R. Bryce and A. P. Monkman, *Adv. Funct. Mater.*, 2009, **19**, 2038.
21 S. Stagni, S. Colella, A. Palazzi, G. Valenti, S. Zacchini, F. Paolucci, M. Marcaccio, R. Q. Albuquerque and L. De Cola, *Inorg. Chem.*, 2008, **47**, 10509.
22 F. De Angelis, S. Fantacci, N. Evans, C. Klein, S. M. Zakeeruddin, J.-E. Moser, K. Kalyanasundaram, H. J. Bolink, M. Grätzel and M. K. Nazeeruddin, *Inorg. Chem.*, 2007, **46**, 5989.
23 R. J. Holmes, S. R. Forrest, T. Sajoto, A. Tamayo, P. I. Djurovich, M. E. Thompson, J. Brooks, Y. J. Tung, B. W. D'Andrade, M. S. Weaver, R. C. Kwong and J. J. Brown, *Appl. Phys. Lett.*, 2005, **87**, 243507.
24 Y. Y. Lyu, Y. Byun, O. Kwon, E. Han, W. S. Jeon, R. R. Das and K. Char, *J. Phys. Chem. B*, 2006, **110**, 10303.
25 A. J. Arduengo, R. L. Harlow and M. Kline, *J. Am. Chem. Soc.*, 1991, **113**, 361.
26 J. C. Garrison and W. J. Youngs, *Chem. Rev.*, 2005, **105**, 3978.
27 M. Gómez-Gallego, M. J. Manchero and M. A. Sierra, *Acc. Chem. Res.*, 2005, **38**, 44.
28 E. O. Fischer and H.-J. Beck, *Angew. Chem., Int. Ed. Engl.*, 1970, **9**, 72.
29 S.-T. Liu and K. R. Reddy, *Chem. Soc. Rev.*, 1999, **28**, 315.
30 F. Kessler, N. Szesni, C. Maaß, C. Hohberger, B. Weibert and H. Fischer, *J. Organomet. Chem.*, 2007, **692**, 3005.
31 C. E. Strasser, E. Stander-Grobler, O. Schuster, S. Cronje and H. G. Raubenheimer, *Eur. J. Inorg. Chem.*, 2009, **2009**, 1905.
32 H. M. J. Wang and I. J. B. Lin, *Organometallics*, 1998, **17**, 972.
33 E. Peris, *Top. Organomet. Chem.*, 2007, **21**, 102.
34 A. K. Verma, J. Singh, V. K. Sankar, R. Chaudhary and R. Chandra, *Tetrahedron Lett.*, 2007, **48**, 4207.
35 A. R. Chianese, P. T. Bremer, C. Wong and R. J. Reynes, *Organometallics*, 2009, **28**, 5244.
36 R. D. Costa, E. Ortí, H. J. Bolink, S. Graber, S. Schaffner, M. Neuburger, C. E. Housecroft and E. C. Constable, *Adv. Funct. Mater.*, 2009, **19**, 3456.
37 Y. Ohsawa, S. Sprouse, K. A. King, M. K. DeArmond, K. W. Hanck and R. J. Watts, *J. Phys. Chem.*, 1987, **91**, 1047.
38 D. L. Davies, M. P. Lowe, K. S. Ryder, K. Singh and S. Singh, *Dalton Trans.*, 2011, **40**, 1028.
39 T. Sajoto, P. I. Djurovich, A. Tamayo, M. Yousufuddin, R. Bau, M. E. Thompson, R. J. Holmes and S. R. Forrest, *Inorg. Chem.*, 2005, **44**, 7992.
40 A. Tsuboyama, H. Iwawaki, M. Furugori, T. Mukaide, J. Kamatani, S. Igawa, T. Moriyama, S. Miura, T. Takiguchi, S. Okada, M. Hoshino and K. Ueno, *J. Am. Chem. Soc.*, 2003, **125**, 12971.
41 S. J. Strickler and R. A. Berg, *J. Chem. Phys.*, 1962, **37**, 814.
42 N. J. Turro, *Modern Molecular Photochemistry*, Mill Valley, CA, 1978.
43 G. Treboux, J. Mizukami, M. Yabe and S. Nakamura, *Chem. Lett.*, 2007, **36**, 1344.
44 T. Sajoto, P. I. Djurovich, A. B. Tamayo, J. Oxgaard, W. A. Goddard and M. E. Thompson, *J. Am. Chem. Soc.*, 2009, **131**, 9813.
45 K. Nozaki, K. Takamori, Y. Nakatsugawa and T. Ohno, *Inorg. Chem.*, 2006, **45**, 6161.
46 F. Alary, J. L. Heully, L. Bijeire and P. Vicendo, *Inorg. Chem.*, 2007, **46**, 3154.
47 J. Van Houten and R. J. Watts, *J. Am. Chem. Soc.*, 1976, **98**, 4853.
48 T. Sajoto, I. Djurovich, A. B. Tamayo, J. Oxgaard, W. A. Goddard and M. E. Thompson, *J. Am. Chem. Soc.*, 2009, **131**, 9813.
49 D. M. Roundhill, *Photochemistry and Photophysics of Metal Complexes*, Plenum, L, 1994.

50 E. Margapoti, V. Shukla, A. Valore, A. Sharma, C. Dragonetti, C. C. Kitts, D. Roberto, M. Murgia, R. Ugo and M. Muccini, *J. Phys. Chem. C*, 2009, **113**, 12517.
51 S. J. Lee, K.-M. Park, K. Yang and Y. Kang, *Inorg. Chem.*, 2009, **48**, 1030.
52 E. Baranoff, S. Suárez, P. Bugnon, H. J. Bolink, C. Klein, R. Scopelliti, L. Zuppiroli, M. Grätzel and M. K. Nazeeruddin, *ChemSusChem*, 2009, **2**, 305.
53 E. Baranoff, J. H. Yum, I. Jung, R. Vulcano, M. Grätzel and M. K. Nazeeruddin, *Chem.–Asian J.*, 2010, **5**, 496.
54 A. J. M. Duisenberg, L. M. J. Kroon-Batenburg and A. M. M. Schreurs, *J. Appl. Crystallogr.*, 2003, **36**, 220.
55 R. H. Blessing, *Acta Crystallogr., Sect. A: Found. Crystallogr.*, 1995, **51**, 33.
56 G. M. Sheldrick, *Acta Crystallogr., Sect. A: Found. Crystallogr.*, 2008, **64**, 112.
57 M. J. Frisch and *et al.*, *Gaussian 2003, Revision D.02*, Wallinford CT, 2004.
58 A. D. Becke, *J. Chem. Phys.*, 1988, **88**, 2547.
59 A. D. Becke, *J. Chem. Phys.*, 1993, **98**, 5648.
60 M. M. Francl, W. J. Pietro, W. J. Hehre, J. S. Binkley, M. S. Gordon, D. J. Defrees and J. A. Pople, *J. Chem. Phys.*, 1982, **77**, 3654.
61 P. J. Hay and W. R. Wadt, *J. Chem. Phys.*, 1985, **82**, 299.
62 C. S. Cramer and D. G. Truhlar, *Solvent Effects and Chemical Reactivity*, Kluwer, Dordrecht, The Netherlands, 1996.
63 J. Tomasi and M. Persico, *Chem. Rev.*, 1994, **94**, 2027.
64 C. Jamorski, M. E. Casida and D. R. Salahub, *J. Chem. Phys.*, 1996, **104**, 5134.
65 M. Petersilka, U. J. Gossmann and E. K. U. Gross, *Phys. Rev. Lett.*, 1996, **76**, 1212.
66 M. E. Casida, C. Jamorski, K. C. Casida and D. R. Salahub, *J. Chem. Phys.*, 1998, **108**, 4439.